




Optimization of seed layer thickness for the growth of the one dimensional vertically oriented ZnO nanowires

Y. K. Abeykoon¹, A. A. I. Lakmal¹, M. A. H. M. Munasinghe³, B. S. Dassanayake^{1,2}, and N. Gunawardhana^{3,*} 

¹Postgraduate Institute of Science, University of Peradeniya, Peradeniya, Sri Lanka

²Department of Physics, Faculty of Science, University of Peradeniya, Peradeniya, Sri Lanka

³Office of Research and International Affairs, Sri Lanka Technological Campus, Padukka, Sri Lanka

Received: 22 July 2022

Accepted: 26 November 2022

Published online:

4 February 2023

© The Author(s), under exclusive licence to Springer Science+Business Media, LLC, part of Springer Nature 2023

ABSTRACT

In this study, ZnO nanowires were grown using chemical bath deposition on top of spray-coated seed layers ranging from 20 to 60 nm in thickness. The effect of seed layer thickness on structural, morphological and optical properties of ZnO nanowires was studied using characterization techniques such as XRD, SEM, and UV–Vis spectroscopy, respectively. The XRD analysis showed that all the nanowires grown on different seed layer thicknesses were hexagonal and preferentially oriented (002) plane. According to the SEM analysis, all the nanowires were vertically oriented. The diameter of the nanowires varied between 47 and 100 nm, and the length ranged typically from 1.03 to 1.78 μm . The bandgap of ZnO nanowires redshift from 2.56 to 3.22 eV with the decrement of seed layer thickness. The H₂ gas sensing behaviour of the fabricated sensor prototype using deposited nanowires was investigated at 150 °C. The optimum response for H₂ gas was obtained for the ZnO nanowires grown on the seed layer thickness of 35 nm.

1 Introduction

Zinc oxide (ZnO) is an n-type semiconductor that possesses a wide direct band gap of 3.37 eV and a large excitation binding energy of 60 meV. Recently, ZnO has received much attention due to its capability to host many different dopant elements [1, 2], one-dimensional (1-D) growth-ability [1–3], and its sensitivity towards synthesizing parameters. With the

advancements in technology, ZnO nanostructures, epitaxial layers, single crystals, and nanoparticles have become promising materials in the production of flat-screen displays, field emission sources [4], gas, chemical and biological sensors [5], UV light emitters [5], optoelectronic (blue and ultraviolet light emitters and detectors) [6], piezoelectric [7] and spintronic devices [8], and solar cells [9].

Address correspondence to E-mail: nandag@sltc.ac.lk

1-D ZnO nanostructures are widely used in photovoltaic and energy conversion devices due to their high surface-to-volume ratio, which enhances the reactivity and improves the absorption of photons, catalytic performance and sensitivity. Hence, 1-D ZnO nanostructures nanobelts [10], nanorods [1, 2], nanowires [1, 11], and nanoflowers [12] have become leading materials in photovoltaics, sensing, and energy conversion devices.

1-D ZnO nanostructures can be synthesized using gas phase and wet chemical methods. Gas-phase methods such as pulsed laser deposition [13], aerosol-assisted chemical vapour deposition [14], and atomic layer deposition [15] require high-temperature conditions over wet chemical methods like sol-gel, electrophoretic deposition [16], microwave radiation-assisted solvothermal [17], hydrothermal [18], and chemical bath deposition techniques [19, 20].

Chemical bath deposition (CBD) is an attractive and cost-effective synthesis method that operates under low-temperature and atmospheric pressure. This can be widely used to deposit sulphides [21, 22], and oxides [23]. CBD mainly depends on a relative solubility product (K_{sp}) [20]. Dissociation of ZnO solid can be given as;



At a given temperature, the ionic product and solubility product can be defined as;

$$\text{Ionic product (IP)} = [\text{Zn}_{(aq)}^{2+}][\text{O}_{(aq)}^{2-}] \quad (2)$$

$$\text{Solubility product (} K_{sp}\text{)} = [\text{Zn}_{(aq)}^{2+}][\text{O}_{(aq)}^{2-}] \quad (3)$$

If $K_{sp} > \text{IP}$, solid phase will dissolve, and precipitation will not occur. When the $K_{sp} = \text{IP}$ solution becomes saturated, the solution will be in equilibrium between the solid and aqueous phase. The solution becomes supersaturated, and precipitation occurs when the $K_{sp} < \text{IP}$. Supersaturated solution undergoes the above-mentioned chemical reactions to form the ZnO solid on the substrate.

CBD is a straightforward method that can be used to synthesize different 1-D nanostructures. Among these, NWs regarded as an attractive nanostructure for the fabrication of photovoltaics, sensing devices etc. The main reason is that NWs have a higher surface-to-volume ratio compared with nanoparticles [24]. Above that, NWs possess several advantageous properties like better crystallinity, well-regulated dimension composition, exceptional Young's

modulus, and the ability to inhibit mechanical degradation [25]. NWs can be fabricated horizontally [26] or vertically [1]. Compared with the horizontally aligned NWs, vertically aligned NWs are high in surface area, as horizontally oriented NWs grow along the substrate while the vertically aligned NWs grow perpendicular to the substrate. In horizontally oriented NWs, lateral growth of NWs becomes dominant over axial growth, while vertically aligned NWs have high axial growth over lateral growth. CBD is widely used to prepare vertically aligned NWs [1–3]. The formation of nucleation sites is essential for the effective growth of vertically oriented NWs. Hence, most researchers apply a seed layer on the substrate before the growth of vertically aligned NWs during CBD.

The seed layer can be a monoatomic layer or a thin film. It creates more nucleation sites to synthesize vertically aligned NWs. During the formation of seed layers, heterogeneous nucleation is more favourable than homogenous nucleation on the foreign surface. Heterogenous nucleation requires less activation energy due to the low contact angle in the liquid–solid interface, hence more favourable in nucleation. Due to lattice mismatch, strain at the interface of growing species, and differential surface energy, it is difficult to control random and complex nucleation processes occurring on a foreign surface. Therefore, the seed layer must be deposited on the substrate with the same material as the nanomaterial grown on the seed layer to support heterogeneous nucleation. This enhances the effective nucleation on favourable sites with minimal surface-free energy [27].

The seed layer is deposited on a substrate using various deposition techniques, including spin coating [2], radio-frequency sputtering (RFsputtering) deposition [28], dip-coating method [1], and Jet Nebuliser Spray Pyrolysis (JNSP) technique [27]. This study used the JNSP technique to apply the seed layer, which is rarely used for seed layer deposition.

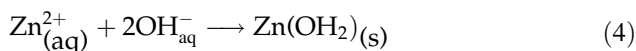
The present work explores the effect of the thickness of the spray-coated seed layer on the growth of the ZnO NWs fabricated through the CBD method. Synthesized NWs were characterized using XRD, SEM, UV–Vis spectroscopy to investigate the structural, morphological and optical properties of the synthesized ZnO NWs. Synthesized NWs were later used for H₂ gas sensing by designing a gas sensor prototype.

2 Materials and methods

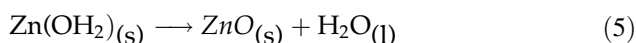
Firstly, borosilicate substrates were cut into 2.5 cm × 2.0 cm pieces and thoroughly cleaned with detergent. Then, they were washed with DI water and dried. After that, the substrates were sonicated in a diluted HCl solution, and the previous step was repeated. Then, the glass plates were cleaned by immersing them in the order of acetone, methanol, and isopropanol just below their respective boiling points. Chemically cleaned substrates were washed with DI water and dried with N₂ before being stored in a desiccator. The substrates were plasma cleaned for 5 min to obtain a better hydrophilic surface.

2.1 Preparation of ZnO seed layers

ZnO seed solution was prepared with 0.1 M solutions of Zinc acetate dehydrate [Zn(CH₃COO)₂·2H₂O—99.5%] with monoethanolamine (MEA) [NH₂CH₂CH₂OH] [2, 3]. The molar ratio between zinc acetate and MEA was 1. Here, MEA was used as a stabilizer. The solution was sonicated for 15 min and stirred for 2 h at 300 rpm and 70 °C. The resulting milky solution was aged for 24 h at room temperature. Following reactions take place during the process;



Upon heating,



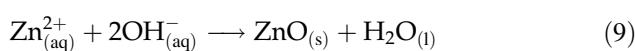
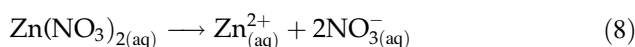
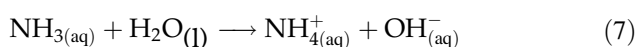
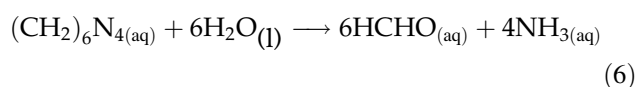
The solution was then spray-coated on the cleaned glass substrate. Throughout the process, the substrate was placed on a hot plate at 120 °C. Layers with 20–60 nm thicknesses were spray-coated on the substrate before 1-min in-situ annealing. The seed layer thickness was optimized by changing the number of seed layers coated onto the substrate.

2.2 Preparation of ZnO NWs

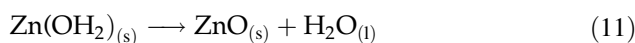
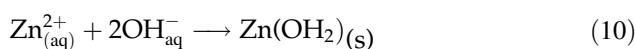
ZnO NWs were grown with an equimolar (0.1 M) aqueous solution of zinc nitrate hexahydrate [Zn(NO₃)₂·6 H₂O—99.5 %] and hexamethylenetetramine (HMTA) [(CH₂)₆N₄—99.5 %]. The prepared substrates with seed layers were used for CBD for 6 h at 90 °C and a rate of 700 rpm. After the CBD process, samples were rinsed with DI water and dried in air.

Finally, the samples were annealed in air at 300 °C for half an hour.

During the CBD process, reactions take place under three steps: (i) creation of atomic/molecular/ionic species, (ii) transportation of species through a medium, and (iii) condensation of the species. Zn(NO₃)₂·6H₂O and HMTA [(CH₂)₆N₄] undergo the following reactions: [3, 19, 29].



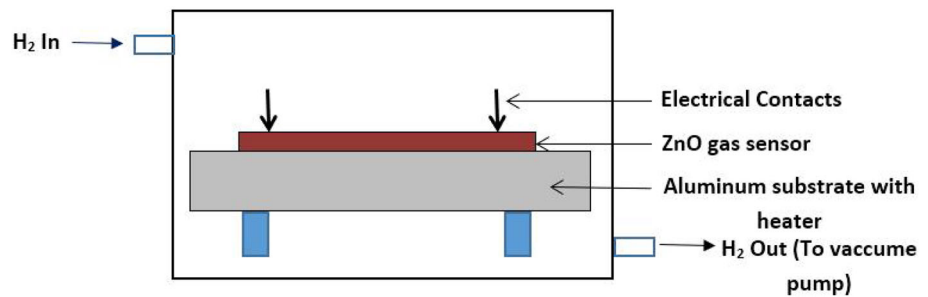
Upon heating, HMTA hydrolyzes to form formaldehyde and NH₃. Then, NH₃ exchanges protons with water molecules providing OH[−]. These hydroxyl ions then react with dissociated Zn²⁺ leading to direct crystallization of ZnO (reaction 9) or indirect crystallization of ZnO (Eqs. 10 and 11) under specific growth conditions.



2.3 H₂ gas sensing

Figure 1 demonstrate an illustration of the gas sensing setup used in the experiment. Cu electrode patterns were thermal evaporated on the top of the ZnO nanowires. Then, the fabricated sensors were kept on an aluminium substrate holder with a heater inside. The temperature was maintained at 150 °C using a PID temperature controller and kept at this temperature until saturation before acquiring data. The Au-coated spring contacts were used to contact Cu electrode patterns. The resistance across the Au contacts was measured with time until the test was completed. The resistance measurements were started before supplying H₂ gas into the chamber and continued until the resistance value became constant and then until it slightly decreased. Then, the H₂ gas supply was terminated, and the remaining gas was removed from the chamber using a vacuum pump while measuring the resistance. The obtained results were converted into responses, and a time vs. response graph was plotted.

Fig. 1 Illustration of gas sensing apparatus used to measure the resistance change of the sensors



2.4 Characterization techniques

The morphology of the deposited seed layers and NWs were studied using the Zeiss EVO LS 15 field emission scanning electron microscope (FESEM). Structural characteristics were investigated using grazing incident X-ray diffractograms (GIXRD) obtained from Bruker D8 Advance with Cu $K\alpha$ ($\lambda = 1.5406 \text{ \AA}$) X-ray photons incident at an angle of 1° and 0.02° intervals from 20° up to 80° . The optical analysis was conducted using a Shimadzu UV-1800 double-beam spectrophotometer.

3 Results and discussion

3.1 Morphological characterization

The SEM images of seed layers deposited using the JNSP method with 5, 10, 15, and 20 seed layer stacks are shown in Fig. 2. The length, morphology, diameter, and surface density of nanowires were examined using these images.

When the seed layer thickness increases, a slight decrement in the size of the seed layer particles (which are the nucleation sites) can be observed until 15 seed layer stacks, reducing the diameter of the NWs. Beyond that, the particle size increased, which resulted in an increased NW diameter. As shown in Table 1, the particle size of the ZnO seed layer with 60 nm is much larger than the rest. Further, a large distribution of the size of nucleation sites can be seen in Fig. 2d, which may be due to the coalescence of nearby smaller nucleation sites.

Figure 3 illustrates the top-down and cross-sectional view of ZnO NWs grown on different seed layers. All ZnO nanowires were grown simultaneously in the same bath using substrates with different numbers of seed layer stacks.

It was observed that while annealing (300°C), the ZnO NWs grown on seed layers tended to fall off the substrate when the number of layer stacks increased beyond 15. The adhesive energy of a thin film or seed layer mainly depends on the residual stress of the film [30]. The adhesive energy decreases with the increase of residual stress. The residual stress of a thin film increases with the thickness and grain size of the thin film [30, 31]. Detachment of the ZnO seed layer and the NWs with increasing seed layer thickness is mainly due to the decrement of the adhesive energy with the increasing residual stress of the seed layer.

It can be seen that the vertical alignment of NWs greatly influenced by the thickness of the NWs. ZnO has polar facets like (0001) and (000 $\bar{1}$) and non-polar facets of (0 $\bar{1}$ 00) and (2 $\bar{1}$ $\bar{1}$ 0). The (0001) surface is terminated with Zn^{2+} ions, while (000 $\bar{1}$) surface is terminated with O^{2-} . Polar facets have about 4 J m^{-2} of surface energy, while non-polar facets have a lower surface energy of about 2 J m^{-2} . Higher surface energy facets react rapidly and attract opposite ions in the solution. Hence, the growth occurs by forming a critical nucleus by secondary nucleation on the surface of polar facets, which reduces the surface energy of the polar surface accordingly. Therefore, NWs growth happens along the c -axis by coordinating with opposite ions by alternatively stacking the zinc and oxygen ion layers. Non-polar surfaces are responsible for the lateral growth of ZnO. Usually, lateral growth is not dominant due to less surface energy of the opposite non-polar surfaces. According to the cross-sectional view, the vertical orientation of NWs strengthens with the increasing thickness of the seed layers, which is in agreement with previous studies [27].

Table 1 also shows the average length, average diameter, and aspect ratio dependence on the ZnO

Fig. 2 The FESEM images of **a** 5, **b** 10, **c** 15, and **d** 20 seed layer stacks grown on borosilicate substrates

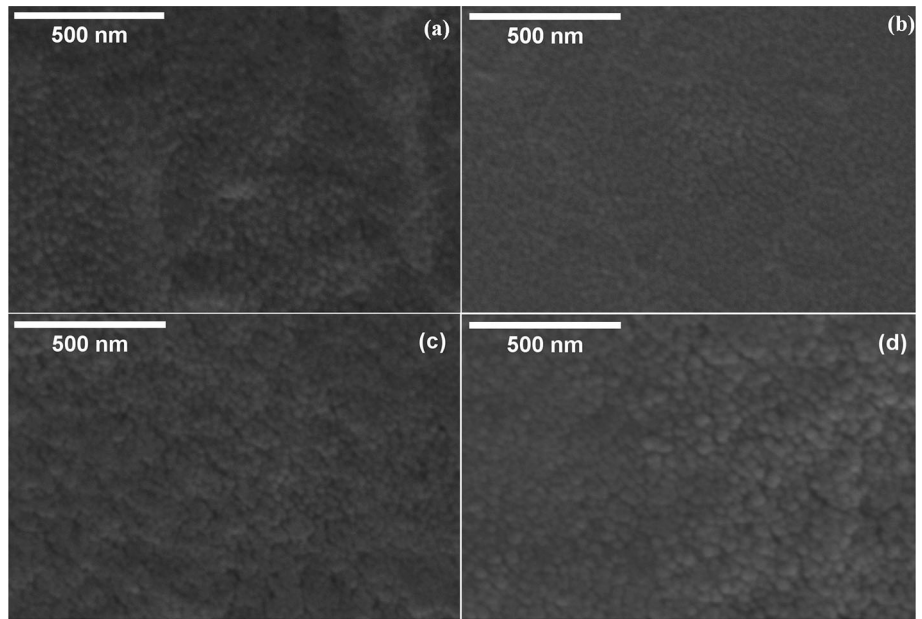
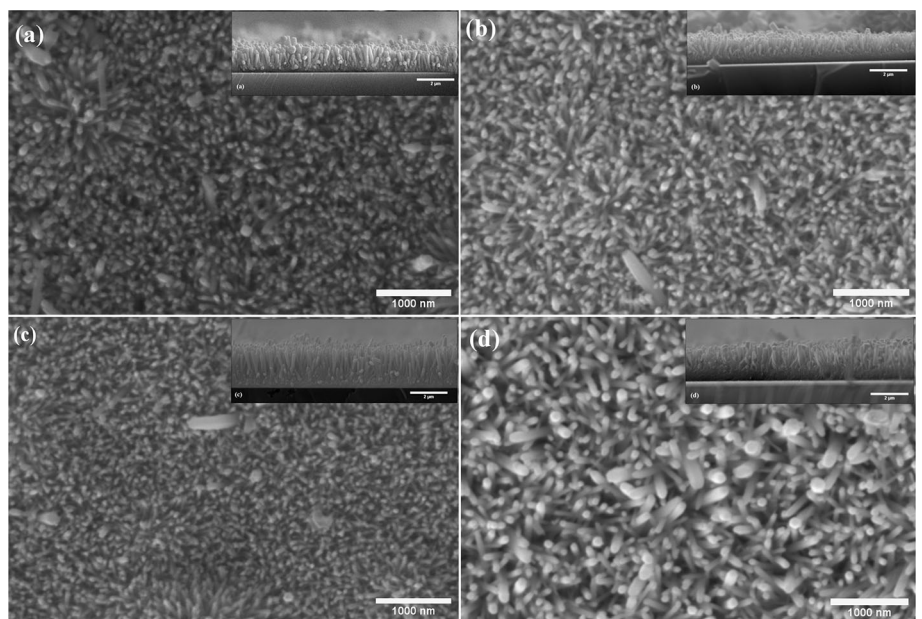


Table 1 Different seed layers and their corresponding NW properties

Number of seed layer stacks	SL thickness (nm)	SL particle size (nm)	NW length (μm)	NW diameter (nm)	Aspect ratio
5	20	23	1.03	59	17.4
10	35	21	1.25	55	22.7
15	50	20	1.78	47	37.9
20	60	35	1.22	100	12.2

Fig. 3 The FESEM images of NWs grown on **a** 5, **b** 10, **c** 15, and **d** 20 seed layer stacks



seed layer thickness. It was found that there was a bit decrement of the NW diameter with the increase in the seed layer thickness until 15 stacks. This can be understood using the grain size of the seed layer ZnO particles. The seed layer provides nucleation sites for the growth of the NWs. The size of the nucleation sites governs the diameter of the NWs grown on the nucleation sites. When the seed layer thickness increases, the size of the seed layer particles slightly decreases, which causes a slight decrement in the diameter of the NWs. In the NWs grown on the 20 seed layer stacks, bigger rods can be seen between the dense smaller rods. One reason for that is the increasing size of the nucleation sites by coalescence of one or more nearby nucleation sites, as previously described. Besides that, Devaraj et al. described this using the lattice orientation effect [27]. According to them, during the growth of ZnO NWs, nucleus formation at the nucleation sites usually occurs along the *c*-axis. If the secondary nucleation takes place during the process, the lattice plane of the growing NW starts to grow parallel to the plane of the nearby NW. Due to the lattice orientation effect, the particles at the interface coalesce along the growth direction throughout the interface. The lateral growth due to the lattice orientation effect leads to the coalescence of nearby NW and the formation of ZnO NWs with larger diameters.

The aspect ratio of the grown NWs increases due to the increment of the NW length with the seed layer thickness, except for the NWs grown on the 20 seed layer stacks. The length of the NWs grown on the 20 seed layer stacks is lower than the NWs grown on 15 and 10 seed layer stacks, according to Table 1. Therefore, the axial growth of NWs grown on 20 seed layer stacks is lower than the NWs grown on 10 and 15 seed layer stacks. When considering the average diameter, the NWs grown on 20 seed layer stacks are larger than the NWs grown on 10 and 15 seed layer stacks. During the same deposition time, the lateral growth of the NWs grown on 20 seed layer stacks is higher than the NWs grown on 10 and 15 seed layer stacks. Accordance to the above fact, the lateral growth has also increased with the axial growth for the NWs grown on 20 seed layer stacks.

As shown in Fig. 4, the density of NWs per unit area increases as the thickness of the ZnO seed layer increases. When the diameter of the NW is small, NWs can be closely packed with each other at the same surface area, which will lead to the increment of

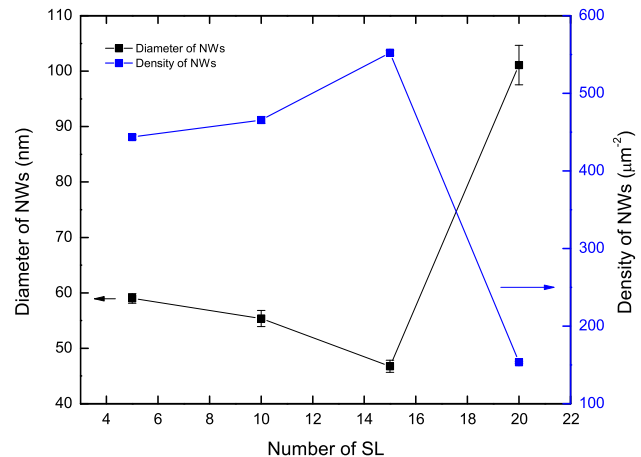


Fig. 4 Changes in density per $1 \mu\text{m}^{-2}$ and an average diameter of ZnO nanowires grown on different seed layers

the NWs per unit area. Thus, the above graph clearly shows that the density of the ZnO nanowires increased as the average diameter decreased. Surface density also describes the richness of the nucleation sites of the seed layers [32]. If the surface NW density is high, then the seed layer has a large number of nucleation sites.

3.2 Optical analysis

Figure 5a and b illustrate the transmittance vs. wavelength spectra in the region of 300–1100 nm in different seed layers and corresponding NWs grown on them. In each transmittance spectra, there is an observable bending between the wavelengths 300 nm to 400 nm responsible for the intrinsic bandgap of ZnO [1, 33]. Optical band gaps of seed layers and ZnO NWs were calculated using Eq. 12, which describes implementing the Tauc method [34].

$$\alpha h\nu = A(h\nu - E_g)^n \quad (12)$$

where α , $h\nu$, A , and E_g are the absorption coefficient, photon energy, relation constant, and optical band-gap, respectively. Since ZnO is a direct bandgap semiconductor, the value of n is equal to 2. Band gaps of the seed layers and deposited nanowires are calculated by extrapolating the Tauc plots.

In both seed layers and NWs, bandgap decreases with increasing seed layer thicknesses, as shown in Table 2. All the seed layers possessed higher band gaps than the bulk ZnO (3.3 eV). However, they decreased with increasing seed layer thickness. Bandgaps of the NWs grown on top of the seed layers

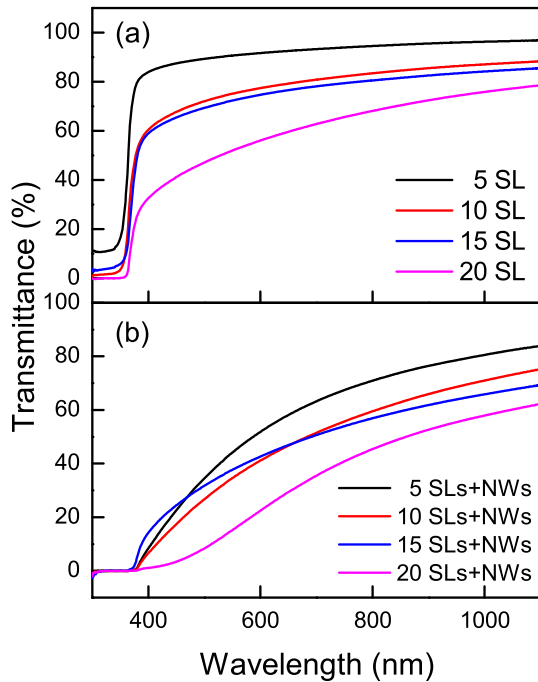


Fig. 5 The UV–Vis spectrum of **a** ZnO seed layers and **b** ZnO nanowires grown on corresponding seed layers

were also found to decrease with seed layer thickness. However, the bandgaps of these NWs were lower than 3.3 eV. All the seed layers and NWs reveal an obvious redshift in their UV transmission. Unsaturated bonds can be produced during the seed layer formation due to the insufficient number of atoms. These unsaturated bonds are responsible for forming defects in the seed layer, leading to localized states. With the increase of seed layer thickness, the width of localized states in the optical band gap increase. Thus, the optical absorption edge decreases, reducing the bandgap. All the seed layers and NWs reveal an obvious redshift in their UV transmission. Unsaturated bonds can be produced during the seed layer formation due to insufficient number of atoms. These unsaturated bonds are responsible for forming defects in the seed layer, leading to localized states.

With the increase of seed layer thickness, the width of localized states in the optical band gap increase. Thus, the optical absorption edge decreases, reducing the bandgap [35–37].

Decrement of the optical absorption edge is mainly due to the increasing defect-induced band tailing effect. The band tailing effect can be calculated using Urbach energy E_U as described in Eq.13. According to Table 2 bandgap of a crystal lattice reduces with the increase of E_U [34, 35].

$$\alpha = \alpha_0 \exp\left(\frac{E - E_g}{E_U}\right) \tag{13}$$

where α_0 is a constant and E is photon energy $h\nu$ and E_U is Urbach energy. E_U was determined by plotting $\ln \alpha$ versus $h\nu$ and linear fitting to the absorption edge. According to the data in Table 2, the bandgaps of seed layers are not mainly affected by E_U . The bandgaps of seed layers decrease with the increase of seed layer thickness due to other defects like particle size, microstrain, or lattice parameters [34]. Overall, bandgap decrement of the NWs with the increment of seed layer thickness is mainly affected by the increment of E_U .

3.3 X-ray diffraction (XRD) analysis

The crystal structure of ZnO NWs was analysed using the X-ray diffraction technique. All the observed diffraction peaks are well-matched with ZnO hexagonal-phase structure (JCPDS No. 36-1451).

Figure 6a–c show the predominant peaks obtained for the seed layers at $2\theta = 31.77^\circ, 34.42^\circ$ and 36.25° are from the (100), (002), (102) planes for the hexagonal ZnO, respectively. According to Fig. 6d–f, intense peaks for NWs were obtained in the above-described planes with 2θ values of $31.80^\circ, 34.52^\circ, 36.3^\circ$. The degree of preferred orientation was quantitatively investigated by calculating the texture coefficient (TC_{hkl}) plotted, as shown in Fig. 7, using Eq. 14 [38];

Table 2 Bandgap and Urbach energy E_U seed layers and corresponding NWs grown on different seed layers

Number of seed layer stacks	Bandgap of the seed layer (eV)	E_U of the seed layer (eV)	Bandgap of NWs (eV)	E_U of NWs (eV)
5	3.41	0.083	3.22	0.147
10	3.40	0.087	3.21	0.161
15	3.39	0.089	3.20	0.284
20	3.38	0.082	2.56	1.173

Fig. 6 GIXRD diffractograms of spray-coated **a** 5, **b** 10, and **c** 15 seed layers and NWs grown on **d** 5, **e** 10, and **f** 15 different seed layers

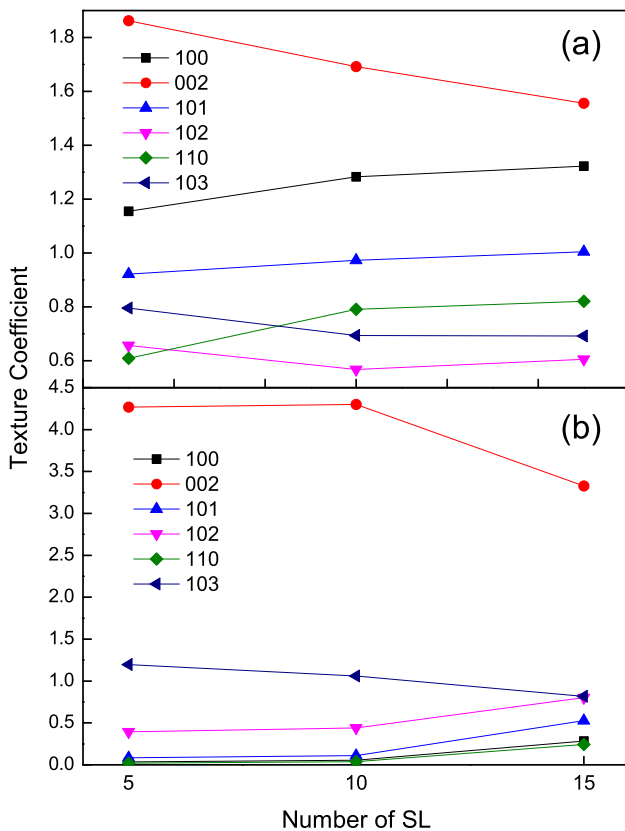
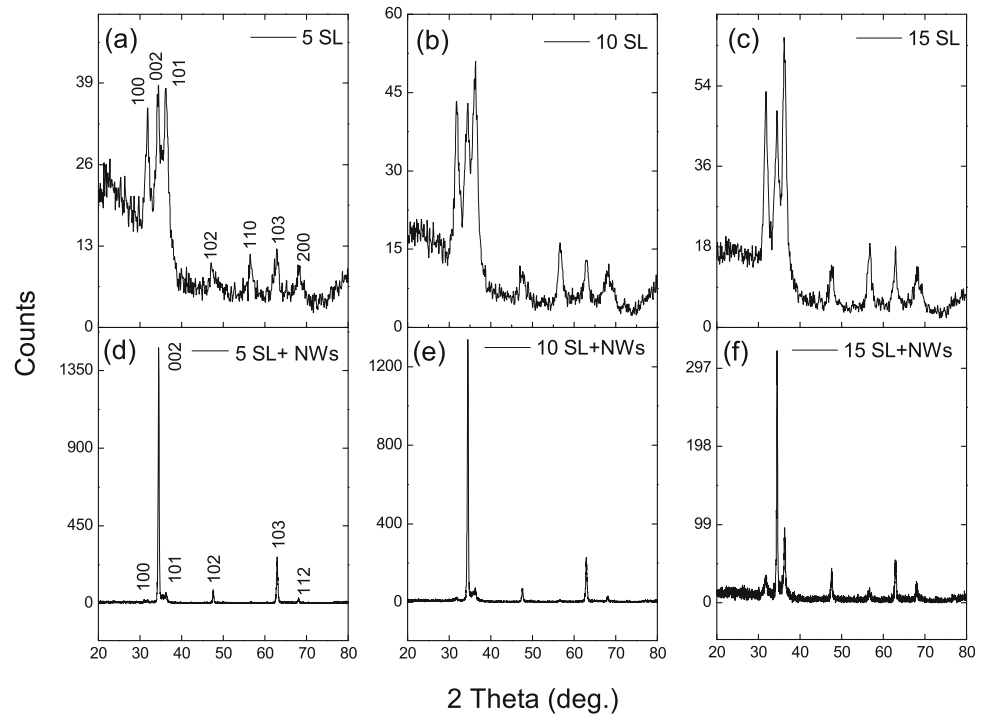


Fig. 7 Texture coefficient variation of **a** different seed layers **b** corresponding NWs

$$TC_{hkl} = \frac{\frac{I_{(hkl)}}{I_{0(hkl)}}}{\frac{1}{N} \sum_N \left(\frac{I_{(hkl)}}{I_{0(hkl)}} \right)} \quad (14)$$

where $I_{(hkl)}$ the Lorentz curve fitted intensity, $I_{0(hkl)}$ is the relative intensity of the corresponding plane given in reference data (PDF 00-041-1049), and N is the number of reflection planes. Here, TC_{hkl} is the measure of the enhancement of the (hkl) reflection compared to a completely randomly oriented sample. The texture coefficient values shown in Fig. 7 reveal that all the seed layers and the corresponding NWs are preferentially oriented in the (002) plane. The decrement of the preferred orientation in the (002) plane is observed with increasing seed layer thickness [39].

Crystallite size of the seed layers and NWs calculated using Debye–Scherrer’s formula [40];

$$D = \frac{0.9\lambda}{\beta \cos\theta} \quad (15)$$

where, D is crystallite size, λ is the wavelength of the X-ray beam, β is the full width at half maximum (FWHM) of the diffraction peak, and θ is the diffraction angle.

As shown in Table 3, the crystallite size of the seed layer increased with seed layer thickness [41], while that of NWs was the opposite. Lattice strain is one of

Table 3 Structural parameters of ZnO seed layers and their corresponding NWs

# Seed layers	D (Å)		ε (%)		a (Å)		c (Å)		Volume (Å ³)	
	SLs	NWs	SLs	NWs	SLs	NWs	SLs	NWs	SLs	NWs
5	56.8	357.3	2.54	0.36	3.241	3.248	5.203	5.201	47.343	47.544
10	51.9	313.1	2.52	0.41	3.240	3.250	5.207	5.199	47.347	47.561
15	63.0	283.6	2.06	0.45	3.244	3.249	5.205	5.205	47.454	47.598

the defects present in the lattice and represents as microstrain (ε). Microstrain can be calculated using Eq. 16; [39, 42–44]

$$\epsilon = \frac{\beta \cos \theta}{4} \tag{16}$$

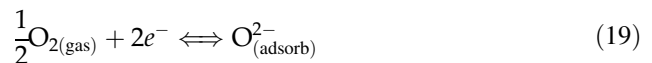
In the seed layers, an increment of seed layer thickness causes the decrement of ε by decreasing the lattice imperfection. But in NWs, ε increases with the seed layer thickness, which causes an increment of the lattice imperfections. Imperfections in lattice or defects lead to the increment of the E_v, lowering the bandgap. Therefore, the observed decrement in the bandgap of NWs in Table 2 can be attributed to the increment in microstrain of NWs [45].

Lattice parameters a, c, and lattice volume were deduced using Pawley unit-cell refinement and tabulated in Table 3 [34, 46]. All the a, and c parameters are in accordance with the JCPDS values of 3.24982 and 5.20661 Å. Results suggest a slight decrement in lattice volume compared to the JCPDS value of 47.62 Å³. In both the seed layers and NWs, lattice volume increases with seed layer thickness. Another reason for the decrement of the band gap of both the seed layers and NWs can be described using lattice volume. The increment of lattice volume can affect the neighbouring atoms to be spread from each other, causing atoms to be loosely packed in the lattice. When the atoms are loosely packed, electron clouds are not attracted much towards the nucleus of the atom. Therefore, valence electrons can be easily removed due to the decrease of binding energy between the nucleus and the electrons of the atoms. Consequently, the energy required to move an electron from the valence band to the conduction band decreases [34]. This will cause the decrement of the bandgap of the seed layers with the increase of seed layer thickness.

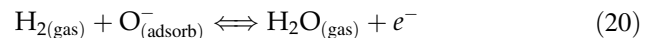
3.4 Gas sensing prototype

3.4.1 Sensing mechanism

At high temperatures, in oxygen ambient, oxygen molecules adsorb to the surface of the sensor. Adsorbed oxygen molecules attract electrons from the conduction band of ZnO and reduce them to form O⁻, and O²⁻ ions, as shown in reactions 15, 16, 17. From these species, O⁻ ions are the most reactive species, which are formed above 100 °C and below 300 °C [47–49]. These ions remain on the surface of the sensor. A decrement in the electron concentration in the conduction band will enhance the resistance of the sensor [47, 50, 51].



When the sensor is exposed to H₂ gas ambient, H₂ gas reacts with O²⁻ and O⁻ ions remaining on the surface, as shown in reaction 18, by releasing electrons back to the conduction band, which increases the concentration of the electrons. This will reduce the resistance of the sensor.



The change in resistance of a sensor for reducing gas like H₂ can be defined as [50, 52];

$$\text{Response (S)} = \frac{R_a}{R_g} \tag{21}$$

where R_a is the electrical resistance of the sensor in the presence of the O₂ gas ambient, and R_g is defined as the sensor’s electrical resistance at the target gas ambient.

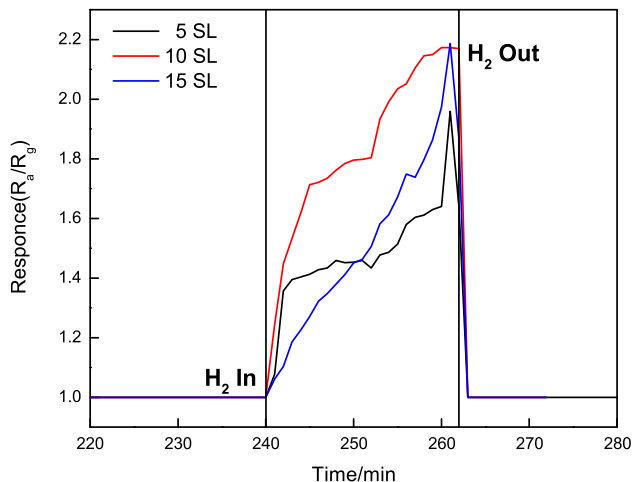


Fig. 8 Response of the ZnO NWs sensors grown on different seed layers when exposed to H₂ with concentration levels of 100 ppm at 150 °C

3.4.2 H₂ gas sensing results

Figure 8 shows the sensing response of the ZnO NWs sensors grown on different seed layers 5, 10, and 15. NWs grown on 20 seed layers were not considered in the gas sensing study since the grown NWs were not adherent to the substrate.

It was observed that the seed layer thickness greatly influences the gas-sensing property of the sensor. As shown in Fig 8, the sensor's response increased with increasing seed layer thickness and obtained the highest response for NWs grown on 15 and 10 seed layers at 150 °C. That is maybe because the surface density of the NWs influenced by the increasing seed layer thickness, as shown in Fig. 4. Within these two prototypes, nanowires grown on a seed layer with 10 layer stacks were shown a higher response over a significant period of time.

4 Conclusion

Hexagonal ZnO nanowires were successfully deposited on the borosilicate glass substrate using the chemical bath deposition technique on top of seed layers with different thicknesses. The optimum morphological properties such as vertical alignment, diameter, length and surface density were observed in the nanowires grown on the seed layer thickness of 50 nm. An increment in the seed layer thickness caused a redshift of the bandgap from 3.22 to 2.56 eV. Optically, the best properties were exhibited by the

ZnO nanowires grown on the seed layer with 20 nm thickness. The ZnO gas sensor prototypes were fabricated successfully using grown ZnO nanowires. The highest response was obtained by the nanowires grown on the seed layer with 35 nm thickness.

Acknowledgements

Financial assistance from Responsive Research Seed Grant of Sri Lanka Technological Campus, Padukka, Sri Lanka (Grant No RRSG/20/A2) is acknowledged. Postgraduate Institute of Science, University of Peradeniya, Sri Lanka, Department of Physics, University of Peradeniya, Sri Lanka are acknowledged for instrumental as well as technical support provided.

Author contributions

YKA: conceptualization, data curation, methodology, investigation, formal analysis, writing—original draft. AAIL: methodology, investigation, formal analysis. MAHMM, NG: conceptualization, investigation, supervision, writing—review & editing, project administration. BSD: conceptualization, investigation, supervision, writing—review & editing.

Data availability

The datasets generated during and/or analysed during the current study are available from the corresponding author on reasonable request

Declarations

Conflict of interest The authors declare that they have no conflict of interest.

References

1. A.H. Rakhsha, H. Abdizadeh, E. Pourshaban, M.R. Golobostanfard, V.R. Mastelaro, M. Montazerian, Ag and Cu doped ZnO nanowires: a pH-controlled synthesis via chemical bath deposition. *Materialia* 5, 100212 (2019). <https://doi.org/10.1016/j.mta.2019.100212>
2. A. Kaphle, M.F. Borunda, P. Hari, Influence of cobalt doping on residual stress in ZnO nanorods. *Mater. Sci. Semicond. Process.* 84, 131–137 (2018). <https://doi.org/10.1016/j.mssp.2018.05.019>

3. M. Poornajar, P. Marashi, D.H. Fatmehsari, M.K. Esfahani, Synthesis of ZnO nanorods via chemical bath deposition method: the effects of physicochemical factors. *Ceram. Int.* **42**(1), 173–184 (2016). <https://doi.org/10.1016/j.ceramint.2015.08.073>
4. L. Liao, J.C. Li, D.F. Wang, C. Liu, C.S. Liu, Q. Fu, L.X. Fan, Field emission property improvement of ZnO nanowires coated with amorphous carbon and carbon nitride films. *Nanotechnology* **16**(6), 985–989 (2005). <https://doi.org/10.1088/0957-4484/16/6/061>
5. X. Fang, Y. Bando, U.K. Gautam, T. Zhai, H. Zeng, X. Xu, M. Liao, D. Golberg, ZnO and ZnS nanostructures: ultraviolet-light emitters, lasers, and sensors. *Crit. Rev. Solid State Mater. Sci.* **34**(3–4), 190–223 (2009). <https://doi.org/10.1080/10408430903245393>
6. T. Gruber, C. Kirchner, K. Thonke, R. Sauer, A. Waag, MOCVD growth of ZnO for optoelectronic applications. *Phys. Status Solidi (a)* **192**(1), 166–170 (2002). [https://doi.org/10.1002/1521-396x\(200207\)192:1<166::aid-pssal166>3.0.co;2-g](https://doi.org/10.1002/1521-396x(200207)192:1<166::aid-pssal166>3.0.co;2-g)
7. L. Jin, L. Li, Quantum simulation of ZnO nanowire piezotronics. *Nano Energy* **15**, 776–781 (2015). <https://doi.org/10.1016/j.nanoen.2015.06.002>
8. F. Pan, C. Song, X.J. Liu, Y.C. Yang, F. Zeng, Ferromagnetism and possible application in spintronics of transition-metal-doped ZnO films. *Mater. Sci. Eng. R* **62**(1), 1–35 (2008). <https://doi.org/10.1016/j.mser.2008.04.002>
9. Q. Zhang, C.S. Dandeneau, X. Zhou, G. Cao, ZnO nanostructures for dye-sensitized solar cells. *Adv. Mater.* **21**(41), 4087–4108 (2009). <https://doi.org/10.1002/adma.200803827>
10. Y. Shi, S. Bao, R. Shi, C. Huang, A. Amini, Z. Wu, L. Zhang, N. Wang, C. Cheng, Y-shaped ZnO nanobelts driven from twinned dislocations. *Sci. Rep.* (2016). <https://doi.org/10.1038/srep22494>
11. K.M. McPeak, J.B. Baxter, ZnO nanowires grown by chemical bath deposition in a continuous flow microreactor. *Cryst. Growth Des.* **9**(10), 4538–4545 (2009). <https://doi.org/10.1021/cg900551f>
12. Y. Qu, R. Huang, W. Qi, M. Shi, R. Su, Z. He, Controllable synthesis of ZnO nanoflowers with structure-dependent photocatalytic activity. *Catal. Today* **355**, 397–407 (2020). <https://doi.org/10.1016/j.cattod.2019.07.056>
13. Y.R. Ryu, S. Zhu, J.D. Budai, H.R. Chandrasekhar, P.F. Miceli, H.W. White, Optical and structural properties of ZnO films deposited on GaAs by pulsed laser deposition. *J. Appl. Phys.* **88**(1), 201–204 (2000). <https://doi.org/10.1063/1.373643>
14. X. Liu, X. Wu, H. Cao, R.P.H. Chang, Growth mechanism and properties of ZnO nanorods synthesized by plasma-enhanced chemical vapor deposition. *J. Appl. Phys.* **95**(6), 3141–3147 (2004). <https://doi.org/10.1063/1.1646440>
15. K.R. Nandanapalli, D. Mudusu, Surface passivated zinc oxide (ZnO) nanorods by atomic layer deposition of ultrathin ZnO layers for energy device applications. *ACS Appl. Nano Mater.* **1**(8), 4083–4091 (2018). <https://doi.org/10.1021/acsnm.8b00816>
16. Y.C. Wang, I.C. Leu, M.H. Hon, Effect of colloid characteristics on the fabrication of ZnO nanowire arrays by electrophoretic deposition. *J. Mater. Chem.* **12**(8), 2439–2444 (2002). <https://doi.org/10.1039/b111189m>
17. C. Min, X. Shen, W. Sheng, Microwave-assisted aqueous synthesis of ultralong ZnO nanowires: photoluminescence and photovoltaic performance for dye-sensitized solar cell. *Appl. Phys. A* **96**(4), 799–803 (2009). <https://doi.org/10.1007/s00339-009-5299-7>
18. H. Hu, X. Huang, C. Deng, X. Chen, Y. Qian, Hydrothermal synthesis of ZnO nanowires and nanobelts on a large scale. *Mater. Chem. Phys.* **106**(1), 58–62 (2007). <https://doi.org/10.1016/j.matchemphys.2007.05.016>
19. R. Parize, J. Garnier, O. Chaix-Pluchery, C. Verrier, E. Appert, V. Consonni, Effects of hexamethylenetetramine on the nucleation and radial growth of ZnO nanowires by chemical bath deposition. *J. Phys. Chem. C* **120**(9), 5242–5250 (2016). <https://doi.org/10.1021/acs.jpcc.6b00479>
20. B.A.E.B.A. Ezekoye, P.O.O.P.O. Offor, V.A.E.V.A. Ezekoye, F.I.E.F.I. Ezema, Chemical bath deposition technique of thin films: a review. *Int. J. Sci. Res.* **2**(8), 452–456 (2012). <https://doi.org/10.15373/22778179/aug2013/149>
21. H. Zhang, X. Ma, J. Xu, J. Niu, J. Sha, D. Yang, Directional cds nanowires fabricated by chemical bath deposition. *J. Cryst. Growth* **246**(1–2), 108–112 (2002). [https://doi.org/10.1016/s0022-0248\(02\)01900-0](https://doi.org/10.1016/s0022-0248(02)01900-0)
22. I.O. Oladeji, L. Chow, A study of the effects of ammonium salts on chemical bath deposited zinc sulfide thin films. *Thin Solid Films* **339**(1–2), 148–153 (1999). [https://doi.org/10.1016/s0040-6090\(98\)01326-1](https://doi.org/10.1016/s0040-6090(98)01326-1)
23. V. Chebrolu, B. B. I. Cho, J.S. Bak, H.J. Kim, The unique core-shell structure of ZnO/NiO heterojunction as an improved performance of supercapacitors via chemical bath deposition approach. *Dalton Trans.* **49**(41), 14432–14444 (2020). <https://doi.org/10.1039/D0DT00263A>
24. I. Udom, M.K. Ram, E.K. Stefanakos, A.F. Hepp, D.Y. Goswami, One dimensional-ZnO nanostructures: synthesis, properties and environmental applications. *Mater. Sci. Semicond. Process.* **16**(6), 2070–2083 (2013). <https://doi.org/10.1016/j.mssp.2013.06.017>
25. K. Yu, X. Pan, G. Zhang, X. Liao, X. Zhou, M. Yan, L. Xu, L. Mai, Nanowires in energy storage devices: structures,

- synthesis, and applications. *Adv. Energy Mater.* **8**(32), 1802369 (2018). <https://doi.org/10.1002/aenm.201802369>
26. B. Nikoobakht, C. Michaels, S. Stranick, M. Vaudin, Horizontal growth and in situ assembly of oriented zinc oxide nanowires. *Appl. Phys. Lett.* **85**(15), 3244–3246 (2004). <https://doi.org/10.1063/1.1803951>
 27. R. Devaraj, K. Venkatachalam, P.M. Razad, Role of seed layer: lattice orientation attachment and structural stabilization on the lateral growth of ZnO nanorods. *J. Mater. Sci.: Mater. Electron.* **27**(4), 4011–4018 (2016). <https://doi.org/10.1007/s10854-015-4255-x>
 28. F.D. Nayeri, E.A. Soleimani, F. Salehi, Synthesis and characterization of ZnO nanowires grown on different seed layers: the application for dye-sensitized solar cells. *Renew. Energy* **60**, 246–255 (2013). <https://doi.org/10.1016/j.renene.2013.05.006>
 29. S.-F. Wang, T.-Y. Tseng, Y.-R. Wang, C.-Y. Wang, H.-C. Lu, W.-L. Shih, Effects of preparation conditions on the growth of ZnO nanorod arrays using aqueous solution method. *Int. J. Appl. Ceram. Technol.* **5**(5), 419–429 (2008). <https://doi.org/10.1111/j.1744-7402.2008.02242.x>
 30. L. Zhang, H. Yang, X. Pang, K. Gao, A.A. Volinsky, Microstructure, residual stress, and fracture of sputtered tin films. *Surf. Coat. Technol.* **224**, 120–125 (2013). <https://doi.org/10.1016/j.surfcoat.2013.03.009>
 31. R. Ali, M. Renzelli, I. Khan, M. Sebastiani, E. Bemporad, Effects of residual stress distribution on interfacial adhesion of magnetron sputtered aln and aln/al nanostructured coatings on a (100) silicon substrate. *Nanomaterials* **8**(11), 896 (2018). <https://doi.org/10.3390/nano8110896>
 32. L.-W. Ji, S.-M. Peng, J.-S. Wu, W.-S. Shih, C.-Z. Wu, I.T. Tang, Effect of seed layer on the growth of well-aligned ZnO nanowires. *J. Phys. Chem. Solids* **70**, 1359–1362 (2009). <https://doi.org/10.1016/j.jpcs.2009.07.029>
 33. D. Dastan, Nanostructured anatase titania thin films prepared by sol-gel dip coating technique. *J. Atom. Mol. Condens. Matter. Nano Phys.* **2**(2), 109–114 (2015)
 34. A.A.I. Lakmal, R.K.K.G.R.G. Kumarasinghe, V.A. Seneviratne, J.Y. Chen, J.M. Song, B.S. Dassanayake, Thermally evaporated cds thin films for cds/cdte solar cells: effect of substrate temperature on cds layer. *Mater. Sci. Eng. B* **273**, 115406 (2021). <https://doi.org/10.1016/j.mseb.2021.115406>
 35. M.B. Rabeh, N. Khedmi, M.A. Fodha, M. Kanzari, The effect of thickness on optical band gap and n-type conductivity of cuins₂ thin films annealed in air atmosphere. *Energy Procedia* **44**, 52–60 (2014). <https://doi.org/10.1016/j.egypro.2013.12.009>
 36. D. Dastan, S.L. Panahi, A.P. Yengntiwar, A.G. Banpurkar, Morphological and electrical studies of titania powder and films grown by aqueous solution method. *Adv. Sci. Lett.* **22**(4), 950–953 (2016). <https://doi.org/10.1166/asl.2016.7130>
 37. D. Dastan, N.B. Chaure, Influence of surfactants on TiO₂ nanoparticles grown by sol-gel technique. *J. Mater. Mech. Manuf.* (2014). <https://doi.org/10.7763/ijmmm.2014.v2.91>
 38. A.A.I. Lakmal, R.K.K.G.R.G. Kumarasinghe, V.A. Seneviratne, M. Thanahaichelvan, B.S. Dassanayake, Effect of CdS layer thickness on thermally evaporated-CdS/CdTe solar cell efficiency. *J. Mater. Sci.: Mater. Electron.* **33**(19), 15627–15637 (2022). <https://doi.org/10.1007/s10854-022-08467-4>
 39. S. Velumani, Structural and optical properties of hot wall deposited cdse thin films. *Sol. Energy Mater. Sol. Cells* **76**(3), 347–358 (2003). [https://doi.org/10.1016/s0927-0248\(02\)00287-8](https://doi.org/10.1016/s0927-0248(02)00287-8)
 40. N.F.A. Rasid, S.N.M. Tawil, N.C. Ani, M.Z. Sahdan, Effect of crystallite size on the optical and structural properties of gadolinium-doped zinc oxide. *Adv. Mater. Res.* **1133**, 414–418 (2016). <https://doi.org/10.4028/www.scientific.net/amr.1133.414>
 41. J. Song, S. Lim, Effect of seed layer on the growth of ZnO nanorods. *J. Phys. Chem. C* **111**(2), 596–600 (2007). <https://doi.org/10.1021/jp0655017>
 42. R. Sathyamoorthy, S. Lalitha, A. Subbarayan, K. Natarajan, Thermally evaporated znpc thin films—band gap dependence on thickness. *Sol Energy Mater. Sol. Cells* **82**(1–2), 179–186 (2004). <https://doi.org/10.1016/j.solmat.2004.01.016>
 43. D. Dastan, Effect of preparation methods on the properties of titania nanoparticles: solvothermal versus sol-gel. *Appl. Phys. A* (2017). <https://doi.org/10.1007/s00339-017-1309-3>
 44. G.-L. Tan, D. Tang, D. Dastan, A. Jafari, J.P.B. Silva, X.-T. Yin, Effect of heat treatment on electrical and surface properties of tungsten oxide thin films grown by hfcdv technique. *Mater. Sci. Semicond. Process.* **122**, 105506 (2021). <https://doi.org/10.1016/j.mssp.2020.105506>
 45. V.K. Peterson, Lattice parameter measurement using le ball versus structural (rietveld) refinement: a caution for complex, low symmetry systems. *Powder Diffr.* **20**(1), 14–17 (2005). <https://doi.org/10.1154/1.1810156>
 46. G.S. Pawley, Unit-cell refinement from powder diffraction scans. *J. Appl. Crystallogr.* **14**(6), 357–361 (1981). <https://doi.org/10.1107/s0021889881009618>
 47. B. Mondal, B. Basumatari, J. Das, C. Roychaudhury, H. Saha, N. Mukherjee, ZnO-SnO₂ based composite type gas sensor for selective hydrogen sensing. *Sens. Actuators B* **194**, 389–396 (2014). <https://doi.org/10.1016/j.snb.2013.12.093>
 48. S. Choopun, N. Hongsih, E. Wongrat, Metal-oxide nanowires for gas sensors. *InTech* (2012). <https://doi.org/10.5772/54385>

49. X.-T. Yin, J. Li, Q. Wang, D. Dastan, Z.-C. Shi, N. Alharbi, H. Garmestani, X.-M. Tan, Y. Liu, X.-G. Ma, Opposite sensing response of heterojunction gas sensors based on SnO₂-Cr₂O₃ nanocomposites to H₂ against CO and its selectivity mechanism. *Langmuir* **37**(46), 13548–13558 (2021). <https://doi.org/10.1021/acs.langmuir.1c01706>
50. J.-H. Kim, A. Mirzaei, H.W. Kim, S.S. Kim, Pd functionalization on ZnO nanowires for enhanced sensitivity and selectivity to hydrogen gas. *Sens. Actuators B* **297**, 126693 (2019). <https://doi.org/10.1016/j.snb.2019.126693>
51. S.M. Beigia, F. Mesgari, M. Hossein, D. Dastan, G. Xu, Electrochemiluminescence sensors based on lanthanide nanomaterials as modifiers. *Curr. Anal. Chem.* **18**(1), 53–62 (2022). <https://doi.org/10.2174/1573411016999200816123009>
52. X.-T. Yin, S.-S. Wu, D. Dastan, S. Nie, Y. Liu, Z.-G. Li, Y.-W. Zhou, J. Li, A. Faik, K. Shan, Z. Shi, M.A. Tarighat, X.-G. Ma, Sensing selectivity of SnO₂-Mn₃O₄ nanocomposite sensors for the detection of H₂ and CO gases. *Surf. Interfaces* **25**, 101190 (2021). <https://doi.org/10.1016/j.surfin.2021.101190>

Publisher's Note Springer Nature remains neutral with regard to jurisdictional claims in published maps and institutional affiliations.

Springer Nature or its licensor (e.g. a society or other partner) holds exclusive rights to this article under a publishing agreement with the author(s) or other rightsholder(s); author self-archiving of the accepted manuscript version of this article is solely governed by the terms of such publishing agreement and applicable law.